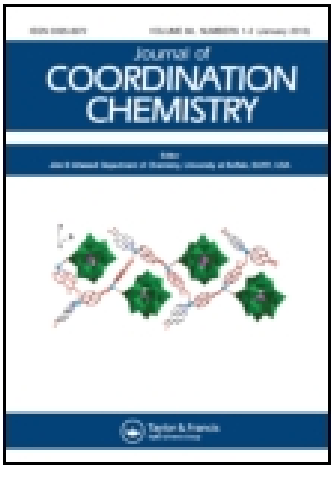

Journal of Coordination Chemistry
Publication details, including instructions for authors and subscription information:
http://www.tandfonline.com/loi/gcoo20

Mimicking the electronic structure of endohedral triangular lanthanide clusters in "free" from host carbon cages metallofullerenes uncovers a peculiar reactivity pattern

Athanassios C. Tsipis[a] & George N. Gkekas[a]
[a] Laboratory of Inorganic and General Chemistry, Department of Chemistry, University of Ioannina, Ioannina, Greece
Accepted author version posted online: 28 Jul 2014.Published online: 18 Aug 2014.

To cite this article: Athanassios C. Tsipis & George N. Gkekas (2014) Mimicking the electronic structure of endohedral triangular lanthanide clusters in "free" from host carbon cages metallofullerenes uncovers a peculiar reactivity pattern, Journal of Coordination Chemistry, 67:15, 2550-2563, DOI: 10.1080/00958972.2014.947969

To link to this article: http://dx.doi.org/10.1080/00958972.2014.947969

Journal of Coordination Chemistry, 2014
Vol. 67, No. 15, 2550–2563, http://dx.doi.org/10.1080/00958972.2014.947969

Mimicking the electronic structure of endohedral triangular lanthanide clusters in "free" from host carbon cages metallofullerenes uncovers a peculiar reactivity pattern

ATHANASSIOS C. TSIPIS* and GEORGE N. GKEKAS

Laboratory of Inorganic and General Chemistry, Department of Chemistry, University of Ioannina, Ioannina, Greece

(*Received 9 May 2014; accepted 27 June 2014*)

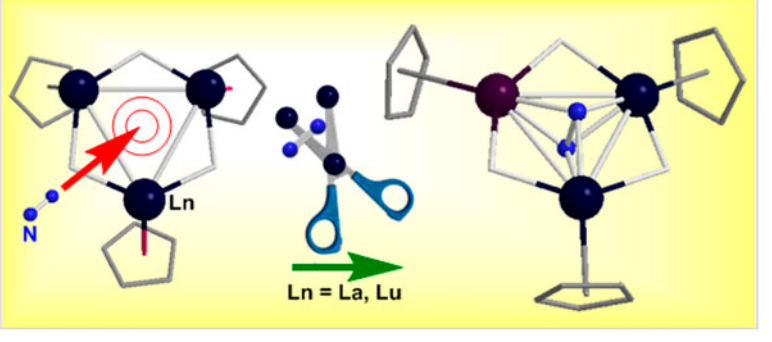

Highly reduced $[Cp_3Ln_3(\mu_2\text{-}H)_3]^{-/0}$ (Ln = La or Lu; Cp = $C_5H_5^-$) clusters "free" from host carbon cages were used as models to mimic the electronic structure of $La_3@C_{110}$ and $Lu_3@C_{80}$ EMFs. DFT calculations revealed that these clusters "unshielded" from host carbon cages are highly reactive, disrupting strong single H–H, H–X (X = F, Cl, Br, and I) and double O=O bonds and descending the inert N≡N triple bond up to a single N–N bond, yielding stable bicapped trinuclear $[Cp_3Ln_3(\mu_2\text{-}H)_3(\mu_3\text{-}H)_2]^-$, $[Cp_3Ln_3(\mu_2\text{-}H)_3(\mu_3\text{-}H)(\mu_3\text{-}X)]^-$, $[Cp_3Ln_3(\mu_2\text{-}H)_3(\mu_3\text{-}O)_2]^-$, and $[Cp_3Ln_3(\mu_2\text{-}H)_3(\mu_3\text{-}N)_2]^-$ clusters. The calculated thermodynamics of the reactions revealed an unprecedented reactivity pattern inherent to multimetallic cooperative effect on nonclassic oxidative addition reactions which proceed by electrophilic attack of the oxidative addition (oxad) substrates at the center of the highly reduced triangular trilanthanide Ln_3 rings accompanied by "penetration" of the ring plane that cuts the strong bonds. The $[Cp_3Ln_3(\mu_2\text{-}H)_3]^{-/0}$ (Ln = La or Lu) clusters, mimicking also the electronic structure of $La_3@C_{110}$ and $Lu_3@C_{80}$ EMFs, easily capture hydrogen, nitrogen, oxygen, and halogen atoms to yield monocapped trimetallic $[Cp_3Ln_3(\mu_2\text{-}H)_3(\mu_3\text{-}X)]$ (X = H, N, O, F, Cl, Br, and I) clusters. The molecular and electronic structures of the "free" from the cage monocapped trimetallic clusters are thoroughly discussed.

Keywords: Triangular La_3 clusters; Triangular Lu_3 clusters; Monocapped triangular lanthanide clusters; Bicapped triangular lanthanide clusters; DFT calculations; Cutting strong bonds

*Corresponding author. Email: attsipis@uoi.gr

1. Introduction

Endohedral metallofullerenes (EMFs) constitute a class of fullerenes which have metal atoms, ions or metallic clusters in their inner space [1–4]. Well-known EMFs are the EMFs of group 3 metals (Sc and Y) and lanthanides. Trimetallofullerenes and particularly the nitride cluster fullerenes (NCFs) have attracted much attention because of their unique electronic structures and bonding features that involve covalent and charge-transfer interactions between the encapsulated metallic species and the carbon cage [1(a)]. EMFs with triangular lanthanide clusters, Ln_3, in the interior of the fullerene cage were also obtained as minor products in the EMFs synthesis, but their structural studies have not been performed [2]. However, a detailed analysis of the intermetallic bonding in the $Y_3@C_{80}$ and $La_3@C_{110}$ by means of electronic structure calculation methods was recently reported [1(c)]. The calculations showed that the $Y_3@C_{80}$ and $La_3@C_{110}$ EMFs adopt a similar bonding pattern based on the interplay of Coulomb repulsion and covalent bonding. Noteworthy the C_{80}^{6-} and C_{110}^{6-} (the $D_3(2355)$ lowest energy C_{110}^{6-} isomer) cages seem to stabilize peculiar electronic states of Y and La corresponding to the unusual +2 oxidation states of the metals. Very recently, the first trimetallofullerene $Sm_3@I_h\text{-}C_{80}$ was reported and characterized experimentally by single-crystal XRD [3]. Computational studies demonstrated that the electronic features of $Sm_3@I_h\text{-}C_{80}$ are similar to those of theoretically studied $Y_3@I_h\text{-}C_{80}$, and both of them have a valence state of $[M_3]^{6+}@[I_h\text{-}C_{80}]^{6-}$. In these two species, the Sm and Y were calculated to adopt a formal +2 oxidation state. Accordingly, it is expected that such highly reduced triangular Y_3, Sm_3, and La_3 clusters are very reactive towards the activation of strong bonds (H–H, H–X, C–X, X–X, O=O, and N≡N, etc.; X = F, Cl, Br, and I) through oxidative addition reactions. However, in endohedral fullerenes, the host carbon cage protects exotic species encapsulated inside, and it is the reason why such exotic structures can be stable. Endohedral species thus cannot exhibit any reactivity because fullerene cage is very stable and completely shields them. Furthermore, these EMFs easily capture highly reactive nitrogen atoms from nitrogen plasma formed into the Krätschmer–Huffman generator used for vaporization of graphite rods containing metal oxides, or from selective nitrogen sources to afford NCFs via oxidative addition reactions for the metals in the NCFs to acquire the more stable +3 oxidation state [1-(d)], but if the EMFs have been firstly encapsulated inside a fullerene cage, it is difficult for an N atom to permeate into the network of fullerene cage and thus it is impossible to form the well-established NCFs.

Very recently, Deng and Popov [4] addressed fundamental questions about the structure and stability of EMFs related to their "ideal" structures and the strain experienced by the clusters encapsulated in the host carbon cages by mimicking the effect of the carbon cages through the coordination of the metal atoms to small organic π-systems (such as pentalene and sumanene). They evaluated the energetic characteristics of the EMF-induced distortions for three classes of EMFs with nitride, sulfide, and carbide clusters and different metals (Sc, Y, and Ti).

To study the reactivity of the endohedral species, which cannot exhibit any reactivity inside the host carbon cages because they are shielded by the host carbon cages, we removed the carbon cage and stabilized the species by coordination of the metal atoms to small organic π-systems, such as the cyclopentadienyl anion ($C_5H_5^-$) resulted in the $[Cp_3Ln_3(\mu_2\text{-}H)_3]^{-/0}$ (Ln = La or Lu; Cp = $C_5H_5^-$) clusters. Considering that the driving force for the reactivity patterns of the $[Cp_3Ln_3(\mu_2\text{-}H)_3]^{-/0}$ clusters might result from the multimetallic cooperative effect, we explored theoretically their ability to activate inert bonds, such as H–H, O=O, and N≡N and H–X (X = F, Cl, Br, and I) through oxidative

addition reactions yielding stable bicapped trinuclear clusters. Interestingly, an unprecedented reactivity pattern related to multimetallic cooperative effect on the oxidative addition reactions that proceed by penetrating the triangular trilanthanide *c*-Ln_3 rings was uncovered. The $[Cp_3Ln_3(\mu_2\text{-}H)_3]^{-/0}$ (Ln = La or Lu) clusters mimicking the electronic structure of $La_3@C_{110}$ and $Lu_3@C_{80}$ EMFs easily capture hydrogen, nitrogen, oxygen, and halogen atoms to yield monocapped trimetallic $[Cp_3Ln_3(\mu_2\text{-}H)_3(\mu_3\text{-}X)]$ (X = H, N, O, F, Cl, Br, and I) clusters. The molecular and electronic structures of the "free" from the cage monocapped trimetallic clusters are also presented herein.

2. Computational details

All structures and energies were calculated using the Gaussian03 suite of programs [5]. Self-consistent field computations were performed with tight convergence criteria on ultrafine grids, while geometry optimizations were converged to tight geometric convergence criteria for all compounds. Structures were considered true minima if they did not exhibit imaginary vibration modes. The PBE0 hybrid functional was used throughout this computational study, since it has already been applied successfully to the description of both energetic and structural aspects of organolanthanide compounds [6]. For geometry optimizations and frequency calculations, the light atoms were treated with 6-311++G(d,p) basis set, whereas the La and Lu atoms were treated with SARC-ZORA basis set [7]. The natural bond orbital (NBO) population analysis was performed using Weinhold's methodology [8]. The electron localization function (ELF) plots were obtained by employing the Multiwfn software version 2.2.1 [9].

3. Results and discussion

3.1. *Equilibrium geometries, bonding, and energetics of the $[Cp_3Ln_3(\mu_2\text{-}H)_3]^{-/0}$ (Ln = La or Lu) clusters*

The optimized geometries with selected structural parameters, the natural atomic charges, and Wiberg Bond Indices (*WBI*) of the anionic $[Cp_3Ln_3(\mu_2\text{-}H)_3]^-$ (Ln = La or Lu) clusters are shown in figure 1. It can be seen that the $[Cp_3Ln_3(\mu_2\text{-}H)_3]^-$ (Ln = La or Lu) clusters adopt a triangular metallic ring core structure with each side of the triangular ring bridged by hydrido ligands. The triangular metallic core exhibits a equilateral triangle geometry with the La–La and Lu–Lu distances of 3.699 and 3.254 Å, respectively. These bond distances are characteristic for single La–La and Lu–Lu bonds (compared with the La–La and Lu–Lu bond distances of 3.247 and 2.938 Å of the single bonds in La_2 and Lu_2 diatomics, respectively) [10]. The La–La and Lu–Lu single bond character is further corroborated by the *WBI* estimated to be 0.941 and 0.982, respectively. The bridged hydrido ligands are located in the vertices of isosceles $Ln_2(\mu_2\text{-}H)$ triangles which are coplanar to the triangular plane. The cyclopentadienyl ligands are coordinated to the lanthanide centers in a η^5-fashion and are bent towards the one side of the $Ln_3(\mu_2\text{-}H)_3$ core plane, leaving the other side open. The $Ln_3(\mu_2\text{-}H)_3$ core plane exhibits negative molecular electrostatic potential (MEP) with a small-sized hole at the ring center (figure 2) and therefore the open side of the ring plane becomes easily susceptible to electrophilic attack by the electrophilic oxad substrates. The 2-D plots of the ELF given in figure 2 clearly indicate the covalent bonding contribu-

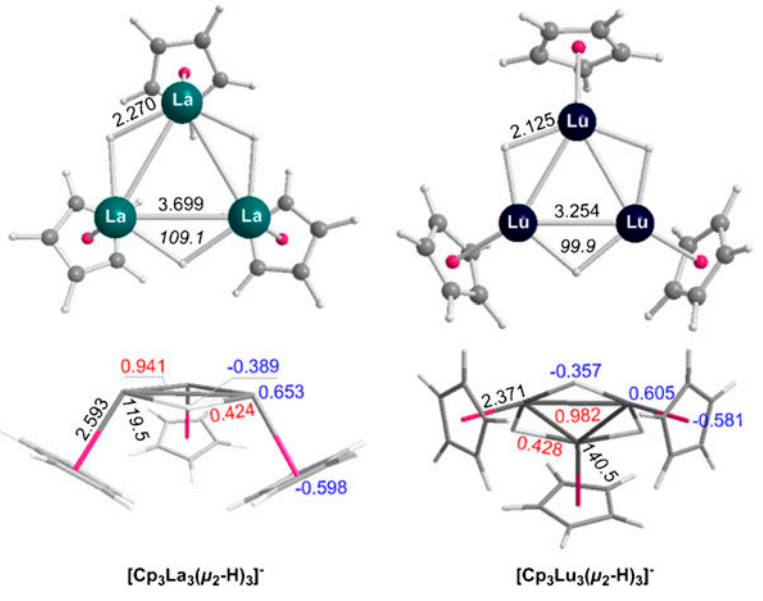

Figure 1. Equilibrium geometries of the anionic triangular $[Cp_3Ln_3(\mu_2\text{-}H)_3]^-$ (Ln = La or Lu) clusters optimized at the PBE0/SARC-ZORA(Ln)U6-311++G(d,p) (E) level. Figures in blue and red are the natural atomic charges and *WBI*, respectively (see http://dx.doi.org/10.1080/00958972.2014.947969 for color version).

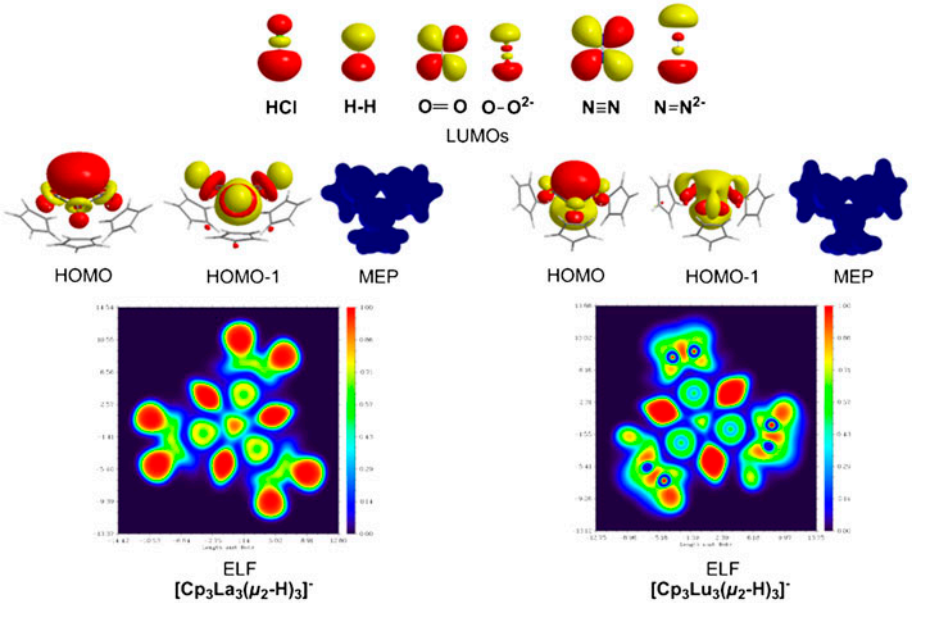

Figure 2. 3-D plots of the highest occupied molecular orbitals (HOMO and HOMO-1), the MEP, and the 2-D plots of the ELF of the anionic triangular $[Cp_3Ln_3(\mu_2 - H)_3]^-$ (Ln = La or Lu) clusters along with the LUMOs of oxidative addition substrates.

tions to the Ln–Ln and Ln–H bonding, the latter dominated by three center-two electron (3c–2e) bonding modes. Noteworthy the anionic triangular $[Cp_3La_3(\mu_2\text{-}H)_3]^-$ and $[Cp_3Lu_3(\mu_2\text{-}H)_3]^-$ clusters are stabilized with respect to their dissociation to monomeric $CpLaH^{0,-}$ and $CpLuH^{0,-}$ species by 140 and 126 kcal M^{-1}, respectively. In other words, the trimerization of the $CpLaH^{0,-}$ and $CpLuH^{0,-}$ species is a thermodynamically favorable process.

Perusal of the frontier molecular orbitals (FMOs) of the triangular $[Cp_3Ln_3(\mu_2\text{-}H)_3]^-$ (Ln = La or Lu) clusters and the oxad substrates (*cf.* figure 2) illustrates that the electrophilic attack of the ring center would be frontier orbital controlled, driven by the HOMO (cluster)-lowest unoccupied molecular orbitals (LUMOs) (oxad substrate) interactions. The $[Cp_3Ln_3(\mu_2\text{-}H)_3]^-$ (Ln = La or Lu) clusters are easily ionized to afford the neutral $[Cp_3Ln_3(\mu_2\text{-}H)_3]$ counterparts in their doublet ground state, the estimated ionization energies are found to be 0.598 and 0.669 eV for the lanthanum and lutetium clusters, respectively. The neutral $[Cp_3Ln_3(\mu_2\text{-}H)_3]$ clusters keep the triangular metallic ring core structure with each side of the triangular ring bridged by hydrido ligands. However, in the neutral species the La–La and Lu–Lu distances are elongated by 0.068 and 0.043 Å, respectively, the La–H and Lu–H bonds are only marginally elongated, while the La–H–La and Lu–H–Lu bond angles are slightly opened by 2.6° and 1.9°, respectively. The weakening of the La–La and Lu–Lu bonds is reflected on the lower *WBI*(Ln–Ln) values of 0.640 and 0.663 in the neutral $[Cp_3La_3(\mu_2\text{-}H)_3]$ and $[Cp_3Lu_3(\mu_2\text{-}H)_3]$ clusters, respectively. The La and Lu atoms in the neutral clusters acquire lower positive natural atomic charges of 0.911 and 0.893 |e|, respectively. The 3-D plots of the spin density given in figure 3 show a uniform distribution of the spin density on the triangular Ln_3 ring, the single electron residing on the singly occupied molecular orbital (SOMO) resulted primarily from the in-phase overlap of the 5*d* AOs of the lanthanide atoms. Noteworthy the nature of the SOMO of the neutral $[Cp_3Ln_3(\mu_2\text{-}H)_3]$ (Ln = La or Lu) clusters favor the SOMO(cluster)-LUMO(oxad substrate) interactions which support the formation of the mono- and bicapped clusters.

The neutral $[Cp_3La_3(\mu_2\text{-}H)_3]$ and $[Cp_3Lu_3(\mu_2\text{-}H)_3]$ clusters are predicted to be bound with respect to their dissociation to monomeric CpLaH and CpLuH species stabilized by 110 and 142 kcal M^{-1}, respectively.

3.2. *Equilibrium geometries, bonding, and energetics of the monocapped $[Cp_3Ln_3(\mu_2\text{-}H)_3(\mu_3\text{-}Y)]$ (Ln = La, Lu; Y = H, O, N) clusters*

The $[Cp_3Ln_3(\mu_2\text{-}H)_3]^{-/0}$ (Ln = La or Lu) clusters used as models of the $La_3@C_{110}$ and $Lu_3@C_{80}$ EMFs easily capture nitrogen atoms to yield trimetallic nitride clusters. The

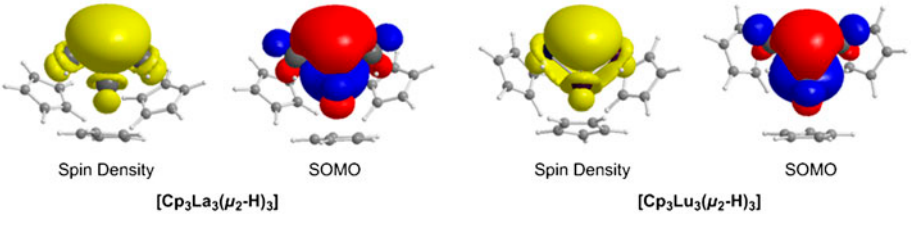

Figure 3. 3-D plots of the spin density and the SOMO of the neutral $[Cp_3Ln_3(\mu_2\text{-}H)_3]$ (Ln = La or Lu) clusters (isospin surface = 0.001).

implantation of the atoms through the walls of the already existing carbon cages is a general method for the preparation of macroscopic amounts of endohedral fullerenes, including ion bombardment, high pressure treatment, or explosion-based implantation [1-(d)]. We studied both the implantation of nitrogen atoms to the neutral $[Cp_3Ln_3(\mu_2\text{-}H)_3]$ (Ln = La or Lu) clusters and the implantation of nitrogen cations to the anionic $[Cp_3Ln_3(\mu_2\text{-}H)_3]^-$ clusters. Both implantation processes are strongly exothermic, the estimated exothermicities are predicted to be 165.4 and 196.8 kcal M^{-1} for the nitrogen atoms implantation to the neutral lanthanum and lutetium clusters, respectively, and 491.0 and 520.8 kcal M^{-1} for the nitrogen cations implantation to the anionic lanthanum and lutetium clusters, respectively (table 1). The much higher exothermicity of the nitrogen cations implantation to the anionic clusters is due to the very strong electrostatic interactions between the anionic cluster and the nitrogen cation. These findings account well for the formation of the NCFs via the nitrogen atom implantation to the already formed $La_3@C_{110}$ and $Lu_3@C_{80}$ EMFs. The implantation of oxygen and hydrogen atoms to the neutral $[Cp_3Ln_3(\mu_2\text{-}H)_3]$ (Ln = La or Lu) clusters and the implantation of oxygen and hydrogen cations to the anionic $[Cp_3Ln_3(\mu_2\text{-}H)_3]^-$ clusters are also predicted to be strongly exothermic processes. The estimated exothermicities for the $[Cp_3Ln_3(\mu_2\text{-}H)_3]([Cp_3Ln_3(\mu_2\text{-}H)_3]^-) + Y(Y^+) \rightarrow [Cp_3Ln_3(\mu_2\text{-}H)_3(\mu_3\text{-}Y)]$ (Y = H, O) processes are given in table 1.

It can be seen that the oxygen atom implantation is the most exothermic, while the hydrogen atom implantation is the least exothermic. Noteworthy all implantation processes studied are more exothermic for the lutetium than the lanthanum clusters. The optimized geometries, with selected structural parameters of the monocapped $[Cp_3Ln_3(\mu_2\text{-}H)_3(\mu_3\text{-}Y)]$ (Ln = La, Lu; Y = H, O, N) clusters, are shown in figure 4.

In all monocapped $[Cp_3Ln_3(\mu_2\text{-}H)_3(\mu_3\text{-}Y)]$ (Ln = La, Lu; Y = H, O, N) clusters, the trimetallic triangle remains equilateral, with the η^5-coordinated cyclopentadienyl ligands being bent towards the one side of the $Ln_3(\mu_2\text{-}H)_3$ core plane as in the case of the triangular $[Cp_3Ln_3(\mu_2\text{-}H)_3]$ (Ln = La or Lu) clusters. Noteworthy the Ln_3Y (Ln = La, Lu; Y = H, O, and N) core structures adopt a trigonal pyramidal structure of C_{3v} symmetry. In the Ln_3Y structures, the estimated La–La distances are shortened by 0.005, 0.093, and 0.060 Å upon capping with N, O, and H, respectively, compared to the La_3 core structures. In the Lu_3N structure the Lu–Lu distance is elongated by 0.037 Å, while it is shortened by 0.057 and 0.049 Å in Lu_3O and Lu_3H core structures, respectively. It is important to notice that the

Table 1. Exothermicities, ΔH of the hydrogen, oxygen, and nitrogen atom or ion implantation to $[Cp_3Ln_3(\mu_2\text{-}H)_3]$ and $[Cp_3Ln_3(\mu_2\text{-}H)_3]^-$ clusters, respectively, calculated at the PBE0/SARC-ZORA (Ln)U6-311++G(d,p) (E) level.

Cluster	Atom or ion	Product	ΔH (kcal M^{-1})
$[Cp_3La_3(\mu_2\text{-}H)_3]$	H	$[Cp_3La_3(\mu_2\text{-}H)_3(\mu_3\text{-}H)]$	−73.8
$[Cp_3La_3(\mu_2\text{-}H)_3]^-$	H^+	$[Cp_3La_3(\mu_2\text{-}H)_3(\mu_3\text{-}H)]$	−373.4
$[Cp_3La_3(\mu_2\text{-}H)_3]$	O	$[Cp_3La_3(\mu_2\text{-}H)_3(\mu_3\text{-}O)]$	−182.4
$[Cp_3La_3(\mu_2\text{-}H)_3]^-$	O^+	$[Cp_3La_3(\mu_2\text{-}H)_3(\mu_3\text{-}O)]$	−584.8
$[Cp_3La_3(\mu_2\text{-}H)_3]$	N	$[Cp_3La_3(\mu_2\text{-}H)_3(\mu_3\text{-}N)]$	−166.6
$[Cp_3La_3(\mu_2\text{-}H)_3]^-$	N^+	$[Cp_3La_3(\mu_2\text{-}H)_3(\mu_3\text{-}N)]$	−492.2
$[Cp_3Lu_3(\mu_2\text{-}H)_3]$	H	$[Cp_3Lu_3(\mu_2\text{-}H)_3(\mu_3\text{-}H)]$	−82.6
$[Cp_3Lu_3(\mu_2\text{-}H)_3]^-$	H^+	$[Cp_3Lu_3(\mu_2\text{-}H)_3(\mu_3\text{-}H)]$	−380.0
$[Cp_3Lu_3(\mu_2\text{-}H)_3]$	O	$[Cp_3Lu_3(\mu_2\text{-}H)_3(\mu_3\text{-}O)]$	
$[Cp_3Lu_3(\mu_2\text{-}H)_3]^-$	O^+	$[Cp_3Lu_3(\mu_2\text{-}H)_3(\mu_3\text{-}O)]$	
$[Cp_3Lu_3(\mu_2\text{-}H)_3]$	N	$[Cp_3Lu_3(\mu_2\text{-}H)_3(\mu_3\text{-}N)]$	−197.9
$[Cp_3Lu_3(\mu_2\text{-}H)_3]^-$	N^+	$[Cp_3Lu_3(\mu_2\text{-}H)_3(\mu_3\text{-}N)]$	−521.7

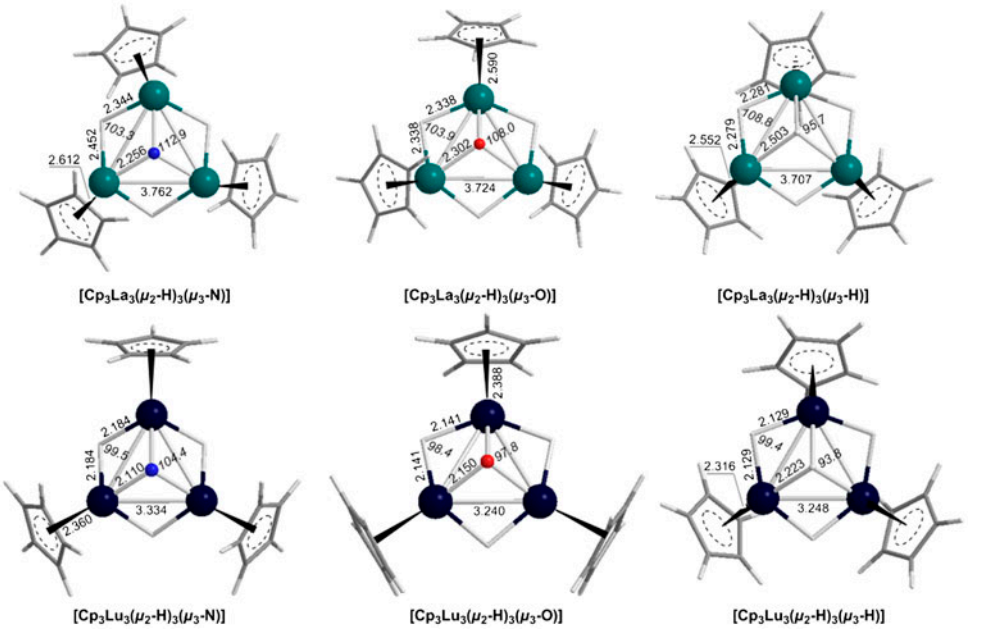

Figure 4. Equilibrium geometries of the monocapped $[Cp_3Ln_3(\mu_2\text{-}H)_3(\mu_3\text{-}Y)]$ (Ln = La, Lu; Y = H, O, and N) clusters optimized at the PBE0/SARC-ZORA(Ln)U6-311++G(d,p) (E) level.

apical position of the trigonal pyramid occupied by N and O atoms is oriented towards the side of the coordinated Cp ligands, while that occupied by H atoms on the opposite side. The pyramidalization (e.g. the separation between the capping atom and the centroid of the triangular ring) in the La_3N, La_3O, and La_3H structural cores are 0.612, 0.904, and 1.292 Å, respectively, whereas in the La_3N, La_3O and La_3H structural cores are 0.864, 1.060, and 1.194 Å, respectively.

Extensive DFT calculations on lanthanide-based $M_3N@C_{88}$ (M = La, Gd, and Lu) revealed that La_3N is the largest and Lu_3N the smallest lanthanide nitride cluster [11]. In these NCFs, La_3N adopts a pyramidal geometry while Lu_3N is nearly planar. The structure of $Lu_3N@C_{80}$ has been examined by single-crystal X-ray diffraction [12], but no X-ray diffraction measurements are available for the La_3N NCFs. The estimated La–La bond distances for the $La_3N@C_{80}$ and $Lu_3N@C_{80}$ NCFs are 3.694 and 3.655 Å, respectively, at the LDA/DND level and 3.728 and 3.675 Å, respectively, at the GGA/DND level. The estimated La-N bond lengths and the pyramidalization are found to be 2.168 and 0.995 Å, respectively. It should be noticed that in the "ligand free" individual La_3N molecule, the La–N bond lengths and the pyramidalization are found to be 2.218 and 1.126 Å, respectively. In the $Lu_3N@C_{80}$ NCFs the Lu–Lu and Lu–N, bond distances determined by X-ray diffraction range from 3.528 to 3.3.554 and from 1.980 to 2.0819 Å, respectively. The structural changes observed in the $[Cp_3Ln_3(\mu_2\text{-}H)_3(\mu_3\text{-}N)]$ clusters could be due to the different coordination environment of the Ln_3N (Ln = La, Lu) structural cores in the $[Cp_3Ln_3(\mu_2\text{-}H)_3(\mu_3\text{-}N)]$ and $Ln_3N@C_{80}$ clusters.

According to NBO analysis (table 2), the lanthanide atoms acquire positive natural atomic charge Q_{Ln} ranging from 0.969 to 1.501 |e|. Q_{Ln} is higher in the $[Cp_3La_3(\mu_2\text{-}H)_3(\mu_3\text{-}Y)]$ than the $[Cp_3Lu_3(\mu_2\text{-}H)_3(\mu_3\text{-}Y)]$ (Y = H, O, and N) clusters and increases going from H

Table 2. Natural atomic charges Q, Wiberg Bond Indices *WBI*, and HOMO–LUMO energy gap (in eV) of the $[Cp_3Ln_3(\mu_2\text{-}H)_3(\mu_3\text{-}X)]$ (Ln = La, Lu; X = H, O, and N) clusters calculated at the PBE0/SARC-ZORA(Ln)U6-311++G(d,p) (E) level.

Cluster	Q_{La}	Q_X	Q_H	Q_{Cp}	*WBI*(Ln–Ln)	*WBI*(La–X)	*WBI*(La–H)	ε_{LUMO}–ε_{HOMO}
$[Cp_3La_3(\mu_2\text{-}H)_3(\mu_3\text{-}H)]$	0.969	−0.351	−0.369	−0.483	0.560	0.288	0.424	1.977
$[Cp_3La_3(\mu_2\text{-}H)_3(\mu_3\text{-}O)]$	1.098	−1.224	−0.405	−0.619	0.545	0.467	0.418	1.114
$[Cp_3La_3(\mu_2\text{-}H)_3(\mu_3\text{-}N)]$	1.501	−1.583	−0.428	−0.545	0.162	0.765	0.400	4.281
$[Cp_3Lu_3(\mu_2\text{-}H)_3(\mu_3\text{-}H)]$	0.913	−0.289	−0.351	−0.466	0.624	0.301	0.430	2.326
$[Cp_3Lu_3(\mu_2\text{-}H)_3(\mu_3\text{-}O)]$	1.046	−1.257	−0.364	−0.596	0.573	0.442	0.421	1.745
$[Cp_3Lu_3(\mu_2\text{-}H)_3(\mu_3\text{-}N)]$	1.388	−1.537	−0.373	−0.503	0.197	0.781	0.418	4.912

to N vertex atom. The increase of Q_{Ln} increases the electrostatic repulsions between the lanthanide atoms, which accounts well for the elongation of the Ln–Ln bond distances along the series of the clusters. The weakening of the Ln–Ln interactions in the $[Cp_3Ln_3(\mu_2\text{-}H)_3(\mu_3\text{-}Y)]$ clusters is also mirrored on the estimated *WBI*(Ln–Ln) values (table 2).

Particularly in the $[Cp_3La_3(\mu_2\text{-}H)_3(\mu_3\text{-}N)]$ and $[Cp_3Lu_3(\mu_2\text{-}H)_3(\mu_3\text{-}N)]$ clusters, the *WBI* (Ln–Ln) values of 0.162 and 0.197 indicate very weak Ln···Ln interactions. The μ_3-Y atoms in the $[Cp_3La_3(\mu_2\text{-}H)_3(\mu_3\text{-}Y)]$ clusters acquire negative natural atomic charges ranging from −0.289 up to −1.583 |e|. Q_Y is higher in the $[Cp_3La_3(\mu_2\text{-}H)_3(\mu_3\text{-}Y)]$ than the $[Cp_3Lu_3(\mu_2\text{-}H)_3(\mu_3\text{-}Y)]$ (Y = H, O, and N) clusters and increases going from H to N vertex atoms. Both the hydrido-bridged and terminal Cp ligands acquire negative natural charges in the range of −0.351 to −0.468 and −0.466 to −0.619 |e|, respectively. Noteworthy the $[Cp_3La_3(\mu_2\text{-}H)_3(\mu_3\text{-}N)]$ clusters exhibiting high HOMO–LUMO energy gap (4.281 and 4.912 eV for the La and Lu clusters, respectively), are expected to be very stable molecules. The less stable $[Cp_3Ln_3(\mu_2\text{-}H)_3(\mu_3\text{-}Y)]$ clusters are predicted to be the $[Cp_3Ln_3(\mu_2\text{-}H)_3(\mu_3\text{-}O)]$ clusters having HOMO–LUMO energy gaps of 1.114 and 1.745 eV for Ln = La and Lu, respectively, followed by the $[Cp_3Ln_3(\mu_2\text{-}H)_3(\mu_3\text{-}H)]$ clusters with HOMO–LUMO energy gaps of 1.977 and 2.326 eV for Ln = La and Lu, respectively.

3.3. *Multimetallic cooperative effect on the oxidative addition of Y_2 (Y = H, O, and N) and H–X (X = F, Cl, Br, and I) to anionic $[Cp_3Ln_3(\mu_2\text{-}H)_3]^-$ (Ln = La, Lu) clusters*

Considering the nature of the FMOs of the highly reduced triangular $[Cp_3Ln_3(\mu_2\text{-}H)_3]^-$ (Ln = La or Lu) clusters and the oxad substrates (*cf.* figure 2) we thought it would be advisable to explore the oxidative addition reactions of the clusters employing Y_2 (Y = H, O, and N) and H–X (X = F, Cl, Br, and I) oxad substrates. Calculations predicted that all oxad reactions studied are strongly exothermic (table 3).

An inspection of table 3 reveals that the oxad reactions of the $[Cp_3Lu_3(\mu_2\text{-}H)_3]^-$ cluster are slightly more exothermic than those of the $[Cp_3La_3(\mu_2\text{-}H)_3]^-$ one. Among the oxad reactions that undergo the anionic triangular $[Cp_3Ln_3(\mu_2\text{-}H)_3]^-$ (Ln = La or Lu) clusters, the less exothermic are the dihydrogen oxidative addition with exothermicities of −43.5 and −57.2 kcal M^{-1}, respectively, and the most exothermic are the dioxygen oxidative addition with exothermicities of −246.2 and −293.5 kcal M^{-1}, respectively. The oxidative addition reactions of H–X (X = F, Cl, Br, and I) and dinitrogen, N_2, to $[Cp_3La_3(\mu_2\text{-}H)_3]^-$ cluster are exothermic by −66.5 to −104.3 kcal M^{-1}, while the corresponding oxad reactions to $[Cp_3Lu_3(\mu_2\text{-}H)_3]^-$ cluster are exothermic by −87.4 to −110.0 kcal M^{-1}.

Table 3. Enthalpy changes, ΔH (in kcal M^{-1}) of the oxidative addition reactions that undergo the anionic triangular $[Cp_3Ln_3(\mu_2\text{-}H)_3]^-$ (Ln = La or Lu) clusters.

Compound	Substrate	Product	ΔH
$[Cp_3La_3(\mu_2\text{-}H)_3]^-$	HF	$[Cp_3La_3(\mu_2\text{-}H)_3(\mu_3\text{-}H)(\mu_3\text{-}F)]^-$	−81.3
	HCl	$[Cp_3La_3(\mu_2\text{-}H)_3(\mu_3\text{-}H)(\mu_3\text{-}Cl)]^-$	−94.9
	HBr	$[Cp_3La_3(\mu_2\text{-}H)_3(\mu_3\text{-}H)(\mu_3\text{-}Br)]^-$	−99.4
	HI	$[Cp_3La_3(\mu_2\text{-}H)_3(\mu_3\text{-}H)(\mu_3\text{-}I)]^-$	−104.3
	H_2	$[Cp_3La_3(\mu_2\text{-}H)_3(\mu_3\text{-}H)_2]^-$	−43.5
	O_2	$[Cp_3La_3(\mu_2\text{-}H)_3(\mu_3\text{-}O)_2]^-$	−246.2
	N_2	$[Cp_3La_3(\mu_2\text{-}H)_3(\mu_3\text{-}N)_2]^-$	−66.5
$[Cp_3Lu_3(\mu_2\text{-}H)_3]^-$	HF	$[Cp_3Lu_3(\mu_2\text{-}H)_3(\mu_3\text{-}H)(\mu_2\text{-}F)]^-$	−102.1
	HCl	$[Cp_3Lu_3(\mu_2\text{-}H)_3(\mu_3\text{-}H)(\mu_2\text{-}Cl)]^-$	−106.7
	HBr	$[Cp_3Lu_3(\mu_2\text{-}H)_3(\mu_3\text{-}H)(\mu_2\text{-}Br)]^-$	−108.3
	HI	$[Cp_3Lu_3(\mu_2\text{-}H)_3(\mu_3\text{-}H)(\mu_2\text{-}I)]^-$	−110.0
	H_2	$[Cp_3Lu_3(\mu_2\text{-}H)_3(\mu_3\text{-}H)_2]^-$	−57.2
	O_2	$[Cp_3Lu_3(\mu_2\text{-}H)_3(\mu_3\text{-}O)_2]^-$	−293.5
	N_2	$[Cp_3Lu_3(\mu_2\text{-}H)_3(\mu_3\text{-}N)_2]^-$	−87.4
	N_2	$[Cp_3Lu_3(\mu_2\text{-}H)_3(\mu_3\text{-}N)(\mu_2\text{-}N)]^-$	−97.2

The optimized geometries of the products of the oxidative addition reactions undergoing the $[Cp_3La_3(\mu_2\text{-}H)_3]^-$ and $[Cp_3Lu_3(\mu_2\text{-}H)_3]^-$ clusters with selected structural parameters along with the natural atomic charges and *WBIs* are shown in figures 5 and 6, respectively.

The electrophilic attack of the triangular ring plane of the $[Cp_3La_3(\mu_2\text{-}H)_3]^-$ cluster by approaching the H–H, O=O, N≡N, and H–X (X=F, Cl, Br, and I) oxad substrates perpendicularly along the z axis results in the complete rupture of the H–H, O=O, and H–X bonds, and the transformation of the triple N≡N to a single N–N bond, with the dissociated atoms capping the triangular lanthanide ring from both sides (μ_3-coordination mode). It seems that along the oxidative addition pathway the H–H, O=O, N≡N, and H-X (X=F, Cl, Br,and I) oxad substrates attacking the ring center "penetrate" the ring plane. In other words the ring plane seems to act as a scissor that cuts the H–H, O=O, and H–X bonds and transforms the triple N≡N to a single N–N bond. This unprecedented reactivity pattern is inherent to multi-metallic cooperative effect on the oxidative addition reactions.

The oxidative addition of the H–X (X=F, Cl, Br, and I) substrates does not affect the $La_3(\mu_2\text{-}H)_3$ core structure (figures 5 and S1, see online supplementary material at http://dx.doi.org/10.1080/00958972.2014.947969). The La_3 triangle remains equilateral, but with edge lengths of 3.645, 3.689, 3.699, and 3.716 Å for the fluoro-, chloro-, bromo-, and iodo-derivatives, respectively. Notice that the edge length of the equilateral triangle in the parent $[Cp_3La_3(\mu_2\text{-}H)_3]^-$ cluster is 3.699 Å (figure 1). The estimated *WBI*(La–La) values around 0.63 indicate the weakening of the La–La bonds with respect to the La–La bonds of the parent $[Cp_3La_3(\mu_2\text{-}H)_3]^-$ cluster. Similarly, in the $[Cp_3La_3(\mu_2\text{-}H)_3(\mu_3\text{-}H)(\mu_3\text{-}X)]^-$ products the $(\mu_2\text{-}H)$La distances are elongated by about 0.05 Å. It is important to be noticed that in the $[Cp_3La_3(\mu_2\text{-}H)_3(\mu_3\text{-}H)(\mu_3\text{-}X)]^-$ products, the position of the Cp ligands adopt almost the perpendicular orientation relative to the $La_3(\mu_2\text{-}H)_3$ core plane. Furthermore, the H···X distances of 2.713, 3.292, 3.448, and 3.671 Å for the F-, Cl-, Br-, and I-derivatives, respectively, illustrate the complete rupture of the H–X bonds. The μ_3-H atom acquires negative natural atomic charge of −0.268 to −0.285 |e|. The same holds true for the μ_3-X atoms that bear negative natural atomic charges of −0.647, −0.395, −0.315, and −0.206 |e| for F, Cl, Br, and I, respectively.

The oxidative addition of the H–H, O=O, and N≡N substrates induce significant structural changes on the $La_3(\mu_2\text{-}H)_3$ core structure (figures 5 and S1 given in SI). The edge lengths of the equilateral triangle are shortened by 0.235 Å in the $[Cp_3La_3(\mu_2\text{-}H)_3(\mu_3\text{-}O)_2]$

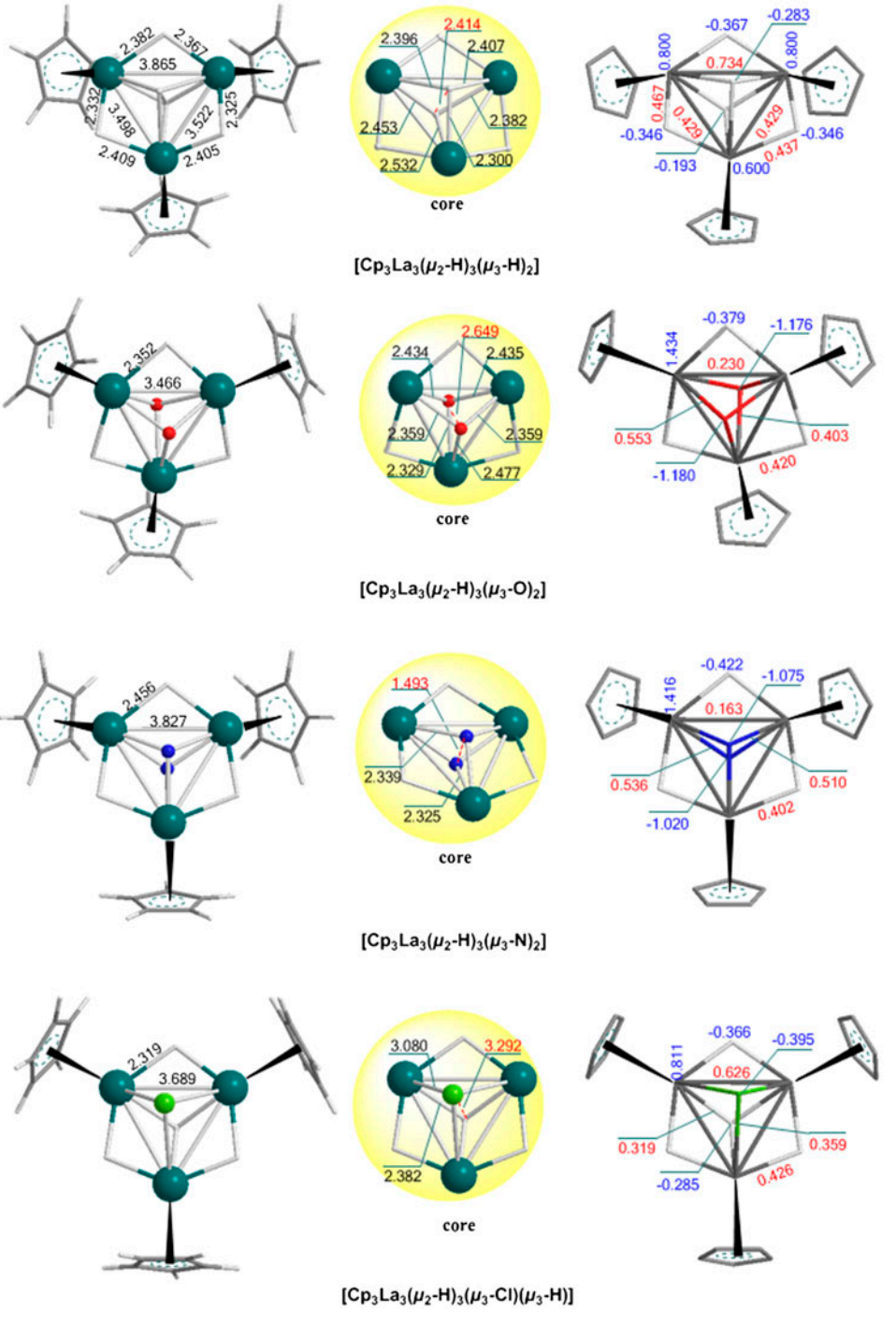

Figure 5. Equilibrium geometries of the oxidative addition products $[Cp_3La_3(\mu_2\text{-}H)_3(\mu_3\text{-}X)_2]^-$ (X=H, O, and N) and $[Cp_3La_3(\mu_2\text{-}H)_3(\mu_3\text{-}H)(\mu_3\text{-}Cl)]^-$ optimized at the PBE0/SARC-ZORA(Ln)U6-311++G(d,p) (E) level. Figures in blue and red are the natural atomic charges and *WBI*, respectively (see http://dx.doi.org/10.1080/00958972.2014.947969 for color version).

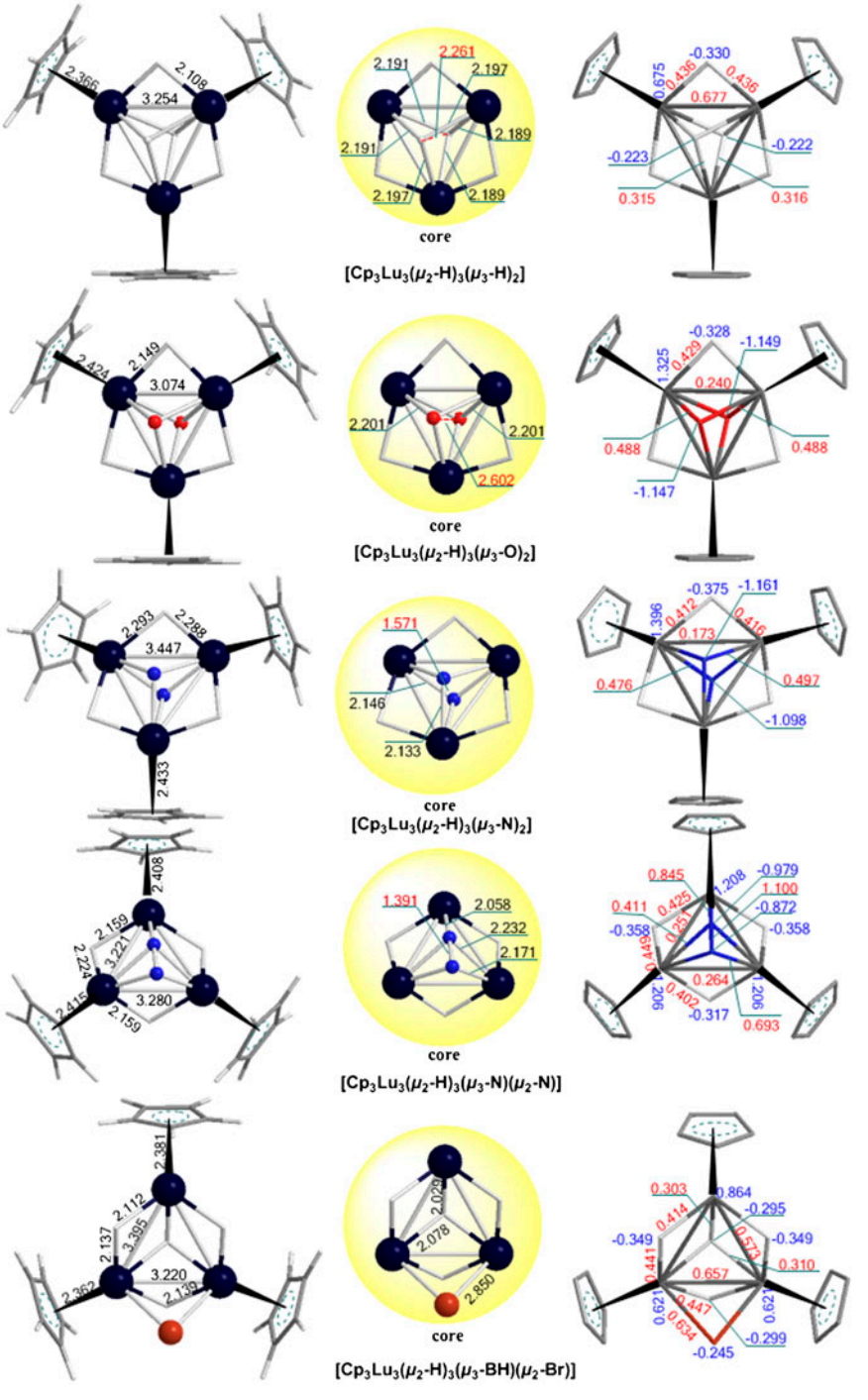

Figure 6. Equilibrium geometries of the oxidative addition products $[Cp_3Lu_3(\mu_2\text{-}H)_3(\mu_3\text{-}X)_3]^-$ (X=H, O, and N) and $[Cp_3Lu_3(\mu_2\text{-}H)_3(\mu_3\text{-}H)(\mu_3\text{-}Br)]^-$ optimized at the PBE0/SARC-ZORA(Ln)U6-311++G(d,p) (E) level. Figures in blue and red are the natural atomic charges and *WBI*, respectively (see http://dx.doi.org/10.1080/00958972.2014.947969 for color version).

cluster but are elongated by 0.128 Å in the $[Cp_3La_3(\mu_2\text{-}H)_3(\mu_3\text{-}N)_2]^-$ one. The estimated $(\mu_2\text{-}H)La$ distances in the $[Cp_3La_3(\mu_2\text{-}H)_3(\mu_3\text{-}O)_2]$ and $[Cp_3La_3(\mu_2\text{-}H)_3(\mu_3\text{-}N)_2]^-$ clusters are elongated by about 0.082 and 0.186 Å, respectively. Noteworthy is the weakening of the La–La bonds, as it is shown by the estimated *WBI*(La–La) values of 0.429, 0.734, 0.230, and 0.163 in the dihydrogen, dioxygen, and dinitrogen activation products, respectively. The H···H, O···O, and N···N distances of 2.414, 2.649, and 1.493 Å, respectively, illustrate the complete rupture of the H–H and O=O bonds and the transformation of the triple N≡N bond to a single N–N bond. The μ_3-H, μ_3-O and μ_3-N atoms acquire negative natural atomic charges of −0.283, −0.193; −1.176, −1.180; −1.075, and −1.020 |e| respectively. Finally, as in the case of the $[Cp_3La_3(\mu_2\text{-}H)_3(\mu_3\text{-}H)(\mu_3\text{-}X)]^-$ products, the position of the Cp ligands in the $[Cp_3La_3(\mu_2\text{-}H)_3(\mu_3\text{-}X)_2]^-$ (X = H, O, and N) products adopts almost the perpendicular orientation relative to the $La_3(\mu_2\text{-}H)_3$ core plane.

The $[Cp_3Lu_3(\mu_2\text{-}H)_3]^-$ cluster was also found to be very reactive towards the activation of inert single, double, and triple bonds, following a similar reactivity pattern inherent to multimetallic cooperative effect on the oxad reactions which involve the penetration of the triangular $Lu_3(\mu_2\text{-}H)_3$ ring.

The oxidative addition of the H–H, O=O, and N≡N substrates does not affect significantly the $Lu_3(\mu_2\text{-}H)_3$ core structure (figure 6). The edge lengths of the equilateral triangle remain unchanged in the $[Cp_3Lu_3(\mu_2\text{-}H)_3(\mu_3\text{-}H)_2]^-$ product, are shortened by 0.180 Å in the $[Cp_3Lu_3(\mu_2\text{-}H)_3(\mu_3\text{-}O)_2]$ cluster, and are elongated by 0.193 Å in the $[Cp_3Lu_3(\mu_2\text{-}H)_3(\mu_3\text{-}N)_2]^-$ product. The estimated $(\mu_2\text{-}H)Lu$ distances in the $[Cp_3Lu_3(\mu_2\text{-}H)_3(\mu_3\text{-}O)_2]$ and $[Cp_3Lu_3(\mu_2\text{-}H)_3(\mu_3\text{-}N)_2]^-$ clusters are elongated by about 0.024 and 0.168 Å, respectively, but the distance is shortened by 0.02 Å in the $[Cp_3Lu_3(\mu_2\text{-}H)_3(\mu_3\text{-}H)_2]^-$ product. The estimated *WBI*(Lu–Lu) values of 0.677, 0.240, and 0.173 indicate the weakening of the Lu–Lu bonds, particularly in the dioxygen and dinitrogen activation products, respectively. The H···H, O···O and N···N distances of 2.261, 2.602, and 1.571 Å, respectively, illustrate the complete rupture of the H–H and O=O bonds and the transformation of the triple N≡N bond to a single N–N bond. The μ_3-H, μ_3-O, and μ_3-N atoms acquire negative natural atomic charges of −0.223; −1.148, and −1.161; and −1.098 |e| respectively indicating that H_2, O_2, and N_2 were subjected to half, two, and four electron reduction. On the other hand, the Lu atoms acquire positive natural atomic charge of 0.675, 1.325 and 1.396 |e| in the dihydrogen, dioxygen, and dinitrogen activation products, respectively. The Cp ligands adopt the perpendicular orientation relative to the $Lu_3(\mu_2\text{-}H)_3$ core plane only in the $[Cp_3Lu_3(\mu_2\text{-}H)_3(\mu_3\text{-}X)_2]^-$ (X = H, O) products. Interestingly, the dinitrogen activation by the $[Cp_3Ln_3(\mu_2\text{-}H)_3]^-$ cluster yielded a product that involves a side-on coordination of dinitrogen. The $[Cp_3Lu_3(\mu_2\text{-}H)_3(\mu_3\text{-}N)(\mu_2\text{-}N)]^-$ product was located as a local minimum on the potential energy surface 9.7 kcal M^{-1} lower in energy than the $[Cp_3Lu_3(\mu_2\text{-}H)_3(\mu_3\text{-}N)_2]^-$ product. It is important to note that in the $[Cp_3Lu_3(\mu_2\text{-}H)_3(\mu_3\text{-}N)(\mu_2\text{-}N)]^-$ product, the La_3 triangle becomes isosceles and the N···N distance predicted to be 1.391 Å is indicative for a dinitrogen bond with partial double-bond character. The partial double-bond character of the side-on coordinated dinitrogen is reflected on the *WBI*(N–N) value of 1.100. The μ_3-N and μ_2-N acquire negative natural atomic charge of −0.979 and −0.872 |e|, respectively, indicating that N_2 undergoes a four electron reduction.

Finally, the oxidative addition of the H–X (X = F, Cl. Br, I) substrates to $[Cp_3Lu_3(\mu_2\text{-}H)_3]^-$ cluster yields the $[Cp_3Lu_3(\mu_2\text{-}H)_3(\mu_3\text{-}H)(\mu_2\text{-}X)]^-$ products (figures 6 and S2 given in SI). In the $[Cp_3Lu_3(\mu_2\text{-}H)_3(\mu_3\text{-}H)(\mu_2\text{-}X)]^-$ products, the Lu_3 triangle becomes isosceles with edge lengths of 3.428, 3.117, 3.403, 3.196, 3.395, 3.220, 3.378, and 3.250 Å for the F-, Cl-, Br-, and I-derivatives, respectively (the shorter edge length corresponds to the basal edge of

the isosceles triangle). Notice that the edge length of the equilateral triangle in the parent $[Cp_3Lu_3(\mu_2\text{-}H)_3]^-$ cluster is 3.254 Å (figure 1). The $[Cp_3Lu_3(\mu_2\text{-}H)_3(\mu_3\text{-}H)(\mu_2\text{-}X)]^-$ products show a remarkable structural difference with respect to the $[Cp_3La_3(\mu_2\text{-}H)_3(\mu_3\text{-}H)(\mu_3\text{-}X)]^-$ products, for the X atom is coordinated to two of the Lu atoms in a μ_2-X coordination mode. The estimated *WBI*(Lu–Lu) values around 0.49–0.66 indicate the weakening of the Lu–Lu bonds with respect to the Lu–Lu bonds of the parent $[Cp_3Lu_3(\mu_2\text{-}H)_3]^-$ cluster and are characteristic of a 3c–2e bonding mode. In the $[Cp_3Lu_3(\mu_2\text{-}H)_3(\mu_3\text{-}H)(\mu_2\text{-}X)]^-$ products, the Cp ligands adopt almost the perpendicular orientation relative to the $Lu_3(\mu_2\text{-}H)_3$ core plane. The estimated H···X distances illustrate the complete rupture of the H-X bonds. Furthermore, the μ_3-H acquires negative natural atomic charge around −0.29 |e|, while the (μ_2-X) atoms also acquire negative natural atomic charges of −0.629, −0.331, −0.245, and −0.106 |e| for F, Cl, Br, and I, respectively.

4. Concluding remarks

Important results are summarized as follows:

The formation of NCFs was modeled employing the $[Cp_3Ln_3(\mu_2\text{-}H)_3]^{-/0}$ (Ln = La or Lu) clusters as models of the $La_3@C_{110}$ and $Lu_3@C_{80}$ EMFs. The $[Cp_3Ln_3(\mu_2\text{-}H)_3]^{-/0}$ (Ln = La or Lu) clusters easily capture nitrogen, oxygen, or hydrogen atoms to yield trimetallic nitride, oxide, and hydride clusters, respectively. The structural and bonding features of the monocapped $[Cp_3Ln_3(\mu_2\text{-}H)_3(Y)]$ (Y = N, O, and H) are thoroughly discussed.

The highly reduced anionic $[Cp_3Ln_3(\mu_2\text{-}H)_3]^-$ (Ln = La or Lu) clusters activate inert bonds through oxidative addition reactions yielding stable bicapped trinuclear clusters. The activation processes constitute an unprecedented reactivity pattern inherent to multimetallic cooperative effect on the oxad reactions that proceed through the penetration of the triangular trilanthanide $Ln_3(\mu_2\text{-}H)_3$ rings. It was found that the $Ln_3(\mu_2\text{-}H)_3$ ring plane acts as a scissor that cuts the inert single and double bonds and transforms the triple to a single bond.

Supplementary material

Equilibrium geometries of the oxidative addition products $[Cp_3La_3(\mu_2\text{-}H)_3(\mu_3\text{-}X)_2]^-$ (Ln = X = F, Br, and I) (figure S1), Equilibrium geometries of the oxidative addition products $[Cp_3Lu_3(\mu_2\text{-}H)_3(\mu_3\text{-}X)_2]^-$ (X = F, Cl, and I) (figure S2), Cartesian Coordinates and energies (in Hartrees) of all clusters (table S1). These data can be obtained free of charge via http://www.ccdc.cam.ac.uk/conts/retrieving.html.

References

[1] (a) M.N. Chaur, F. Melin, A.L. Ortiz, L. Echegoyen. *Angew. Chem., Int. Ed.*, **48**, 7514 (2009); (b) A. Rodriguez-Fortea, A.L. Balch, J.M. Poblet. *Chem. Soc. Rev.*, **40**, 3551 (2011); (c) A.A. Popov, S.M. Avdoshenko, A. Pendas, L. Dunsch. *Chem. Commun.*, **48**, 8031 (2012); (d) A.A. Popov, S.F. Yang, L. Dunsch. *Chem. Rev.*, **113**, 5989 (2013).

[2] (a) S.F. Yang, L. Dunsch. *Angew. Chem., Int. Ed.*, **45**, 1299 (2006); (b) N. Tagmatarchis, E. Aslanis, K. Prassides, H. Shinohara. *Chem. Mater.*, **13**, 2374 (2001); (c) Y.F. Lian, Z.J. Shi, X.H. Zhou, Z.N. Gu. *Chem. Mater.*, **16**, 1704 (2004); (d) A.A. Popov, L. Zhang, L. Dunsch. *ACS Nano*, **4**, 795 (2010).

[3] W. Xu, L. Feng, M. Calvaresi, J. Liu, Y. Liu, B. Niu, Z.J. Shi, Y.F. Lian, F. Zerbetto. *J. Am. Chem. Soc.*, **135**, 4187 (2013).
[4] Q. Deng, A.A. Popov. *J. Am. Chem. Soc.*, **136**, 4257 (2014).
[5] M.J. Frisch, G.W. Trucks, H.B. Schlegel, G.E. Scuseria, M.A. Robb, J.R. Cheeseman, J.A. Montgomery, Jr., T. Vreven, K.N. Kudin, J.C. Burant, J.M. Millam, S.S. Iyengar, J. Tomasi, V. Barone, B. Mennucci, M. Cossi, G. Scalmani, N. Rega, G.A. Petersson, H. Nakatsuji, M. Hada, M. Ehara, K. Toyota, R. Fukuda, J. Hasegawa, M. Ishida, T. Nakajima, Y. Honda, O. Kitao, H. Nakai, M. Klene, X. Li, J.E. Knox, H.P. Hratchian, J.B. Cross, V. Bakken, C. Adamo, J. Jaramillo, R. Gomperts, R.E. Stratmann, O. Yazyev, A.J. Austin, R. Cammi, C. Pomelli, J.W. Ochterski, P.Y. Ayala, K. Morokuma, G.A. Voth, P. Salvador, J.J. Dannenberg, V.G. Zakrzewski, S. Dapprich, A.D. Daniels, M.C. Strain, O. Farkas, D.K. Malick, A.D. Rabuck, K. Raghavachari, J.B. Foresman, J.V. Ortiz, Q. Cui, A.G. Baboul, S. Clifford, J. Cioslowski, B.B. Stefanov, G. Liu, A. Liashenko,
P. Piskorz, I. Komaromi, R.L. Martin, D.J. Fox, T. Keith, M.A. Al-Laham, C.Y. Peng, A. Nanayakkara, M. Challacombe, P.M.W. Gill, B. Johnson, W. Chen, M.W. Wong, C. Gonzalez, J.A. Pople, *Gaussian 03, Revision E.01*, Gaussian, Inc., Wallingford, CT (2004).
[6] (a) M. Ernzerhof, G.E. Scuseria. *J. Chem. Phys.*, **110**, 5029 (1999); (b) C. Adamo, V. Barone. *Chem. Phys. Lett.*, **274**, 242 (1997); (c) C. Adamo, V. Barone. *J. Chem. Phys.*, **110**, 6160 (1999); (d) C. Adamo, G.E. Scuseria, V. Barone. *J. Chem. Phys.*, **111**, 2889 (1999); (e) C. Adamo, V. Barone. *Theor. Chem. Acc.*, **105**, 169 (2000); (f) V. Veter, C. Adamo, P. Maldivi. *Chem. Phys. Lett.*, **325**, 99 (2000); (g) C. Adamo, V. Barone. *J. Comput. Chem.*, **21**, 1153 (2000); (h) X. Wang, L. Andrews, I. Infante, L. Gagliardi. *J. Phys. Chem. A*, **113**, 12566 (2009); (i) B. Vlaisavljevich, P. Miro, C.J. Cramer, L. Gagliardi, I. Infante, S.T. Liddle. *Chem. Eur. J.*, **17**, 8424 (2011); (j) M.J. Polinski, D.J. Grant, S. Wang, E.V. Alekseev, J.N. Cross, E.M. Villa, W. Depmeier, L. Gagliardi, T.E. Albrecht-Schmitt. *J. Am. Chem. Soc.*, **134**, 10682 (2012).
[7] (a) D.E. Pantazis, F. Neese. *J. Chem. Theory Comput.*, **5**, 2229 (2009); (b) EMSL basis set exchange. Available online at: https://bse.pnl.gov/bse/portal (accessed 05 March 2013).
[8] (a) A.E. Reed, L.A. Curtiss, F. Weinhold. *Chem. Rev.*, **88**, 899 (1998); (b) F. Weinhold, In *The Encyclopedia of Computational Chemistry*, P.V.R. Schleyer (Ed.), pp. 1792–1811, John Wiley & Sons, Chichester (1998).
[9] T. Lu, F. Chen. *J. Comput. Chem.*, **33**, 580 (2012).
[10] M. Dolg, H. Stoll, H. Preuss. *J. Mol. Struct. (Theochem)*, **277**, 239 (1992).
[11] L. Xu, S.-F. Li, L.-H. Gan, C.-Y. Shu, C.-R. Wang. *Chem. Phys. Lett.*, **521**, 81 (2012).
[12] S. Stevenson, H.M. Lee, M.M. Olmstead, C. Kozikowski, P. Stevenson, A.L. Balch. *Chem. Eur. J.*, **8**, 4528 (2002).